MRI investigation of subcellular water compartmentalization and gas distribution in apples

G. Winisdorffer, Maja Musse, S. Quellec, M.F. Devaux, Marc Lahaye, François Mariette

Elsevier Editorial System(tm) for Magnetic Resonance Imaging
Manuscript Draft

Manuscript Number: MRI-D-14-00149R1

Title: MRI investigation of subcellular water compartmentalization and gas distribution in apples

Article Type: Original Contribution

Keywords: Multi-exponential transverse (T2) relaxation; microporosity; macrovision; apple parenchyma tissue

Corresponding Author: Dr. Maja Musse, PHD

Corresponding Author's Institution: IRSTEA

First Author: Guillaume Winisdorffer

Order of Authors: Guillaume Winisdorffer; Maja Musse, Ph.D; Stéphane Quellec; Devaux Marie-Françoise, Ph.D; Marc Lahaye, Ph.D; François Mariette, Ph.D

Abstract

Water status and distribution at subcellular level in whole apple fruit were evaluated by Magnetic Resonance Imaging (MRI) measurement of the multi-exponential transverse (T_2) relaxation of water protons. Apparent microporosity, also estimated by MRI, provided mapping of gas distribution in fruit tissues. Measuring for the first time the multi-exponential relaxation of water and apparent tissue microporosity in whole fruit and combining these with histological measurements provided a more reliable interpretation of the origins of variations in the transverse relaxation time (T_2) and better characterization of the fruit tissue. Measurements were performed on 54 fruit from 3 different cultivars. Fruit of different sizes were selected for each cultivar to provide tissues with cells of different dimensions. Macrovision measurements were carried out on parenchymal tissue from all fruit to investigate the impact of cell morphology and cell size of all samples on T_2 value.

The results showed that the MRI transverse relaxation signal is well fitted by a tri-exponential decay curve that reflects cell compartmentalization. Variations in cell size partially explained the different T_2 observed. This study highlighted the heterogeneity of apple tissues in terms of relaxation parameters, apparent microporosity and cell morphology and in relation to specific variations between fruit of different cultivars.

1 Introduction

Apple fruit has been widely studied because of its economic importance. Among the different tissues making up this fleshy fruit (Fig. 1), the parenchyma is very important as it is the main consumable part. Its texture depends on cellular structure and organization as well as on the biochemical composition of the tissue [1]. The histological features of the apple parenchyma have already been described [2,3]; parenchyma cells situated immediately under the cuticle are relatively small and round. Cells rapidly increase in size in the first millimeters under the cuticle and then elongate with distance from the cuticle. As for many fleshy fruit, the size of the apple fruit depends on cell number and cell size [4-6]. In addition to cells, the apple parenchyma contains intercellular spaces that form pores, increasing in occurrence towards the cuticle, except for the region immediately under it [3,7]. This microporosity increases with fruit size [6] though it appears to be related to orchard management [8].

Nuclear Magnetic Resonance (NMR) relaxation and Magnetic Resonance Imaging (MRI) have been used in several studies to investigate water in plant tissues [9]. The NMR signal of water is characterized by longitudinal (T_1) and transverse (T_2) relaxation times that are governed by contributions from different factors [10,11]. First, bulk relaxation is related to the mobility of water and is affected by the chemical exchange of water protons with macromolecules and solid surfaces. Water in different cell compartments thus has different bulk relaxation times due to distinct concentrations and the nature of osmolites. Secondly, relaxation times are modified by diffusional exchange of molecules between compartments through permeable membranes. In the case of slow diffusional exchange, the resulting water relaxation signal is multi-exponential, reflecting water compartmentalization. Three or four components have been obtained in the apple, depending on the NMR protocol. These have been assigned to the vacuole, the cytoplasm and the wall/extracellular water [12-14]. NMR

relaxation measurements can be used to estimate the relative proportions and the properties of water in different compartments. T_2 relaxation time is used for plant cell investigations rather than T_1, as differences in T_2 are more pronounced for the different cell compartments [10]. Due to the contributions of the different factors described above, compartment size affects T_2 relaxation times [15,16]. According to the NMR relaxation model in porous media adapted by Van Der Weerd et al. to plant cells, the T_2 of water ($T_{2,obs}$) confined in a vacuolar compartment can be defined as a function of the bulk T_2 ($T_{2,bulk}$), the radii of the vacuole along spatial directions (R_x, R_y, R_z) and the sink strength (H) describing the rate of the loss of magnetization at the membrane boundary:

$$\frac{1}{T_{2,obs}} = H\left(\frac{1}{R_x} + \frac{1}{R_y} + \frac{1}{R_z}\right) + \frac{1}{T_{2,bulk}} \qquad \text{Eq. (1)}$$

In general, H is affected by the exchange of water with molecules from an adjacent compartment with different T_2 through the permeable membrane, and by direct interaction with the membrane acting as a sink for relaxation. The wide variation in cell size in pearl millet and maize stems allowed the demonstration of Eq. (1) for plant cells, assuming that the mono-exponential adjustment of the T_2 relaxation curve reflects only the T_2 from the vacuole compartment [16].

In addition to the complexity of the phenomena that affect T_2 values, other mechanisms also modulate the T_2 measured [17]. The latter is reduced by diffusion in the presence of random field gradients generated by susceptibility inhomogeneities and, in the case of MRI measurement, by diffusion in the presence of imaging gradients [17,18]. In fruit, the magnetic susceptibility inhomogeneities originate mainly from gas associated with the microporosity of the sample; this is accentuated at higher magnetic fields and has to be considered in interpretation of the T_2 since considerable reduction in the T_2 has been recorded with increased magnetic field strength [18,19].

MRI studies of apples reported in the literature have mainly focused on the development of techniques for detection of metabolic disorders and the non-destructive nature of the method has been particularly highlighted. T_2 has been used as a local marker of tissue modification [20,21] and T_2 weighted images or T_2 maps have therefore been established in apples to study fruit quality and defects and as a probe for defects happening over time. For example, development of watercore [22-24] and internal browning [22,25,26], both linked to changes in microstructure implying flooding of intercellular pores [7,27,28] and collapse of cell wall and cells for browning disorder [29], were at the origin of changes in T_2. Mealiness was also linked to changes in relaxation times [30-32]. The use of a T_2 map to study the microstructural heterogeneity of healthy apple parenchyma has been less widely explored. This aspect was recently addressed by Defraeye et al. [33] in measuring T_2 in regions of interest in parenchyma and core tissues and showed differences in T_2 between the two tissues. T_2 was also used to extract quantitative information in the recently proposed method for measurements of microporosity [19]. This method exploits the susceptibility effects induced by small gas bubbles on the MRI relaxation signal. Using a combination of T_2 and T_2^* maps, Musse et al. showed that a microporosity map can be quantified in fruit.

All MRI T_2 mapping on fruit to date has been limited to the estimation of mono-exponential relaxation. An MRI method allowing assessment of spatially resolved multi-exponential T_2 has recently been proposed [34] and applied to apples. Using this MRI method, the multi-exponential T_2 and their relative amplitudes can be directly computed in different regions of interest.

The techniques commonly used for the analysis of fruit tissue structure (i.e. microscopy and X-ray microtomography) have a local character and therefore do not provide a global view of the whole fruit. Additional spatially resolved information on the relative proportions and properties of water in cell compartments and on the microporosity of tissues

would therefore increase understanding of fruit microstructure and help to understand factors affecting its texture. The main aim of the study presented here was to evaluate the microstructure of apple parenchyma via spatially resolved multi-exponential T_2 relaxation measurements. As apple tissue is known to be very porous, microporosity maps were computed and considered in the analyses of relaxation parameters. The sensitivity of T_2 to the cell dimensions in the range of cell sizes found in apple parenchyma was investigated to improve our understanding of the MRI signal in fruit. The second aim was to investigate variations in both T_2 and microporosity inside apple fruit, with a focus on the parenchyma tissues. Multi-exponential T_2 and microporosity maps were established in 54 fruit from 3 different cultivars. Fruit of different sizes were selected for each cultivar to provide cells of different dimensions. Macrovision measurements [35] were carried out on all fruit to investigate cell morphology and to estimate the cell size of the samples.

2 Materials and Methods

1. Fruit and sampling

Apples were studied from three different cultivars (Fuji, Ariane, Jonagored) harvested at maturity. Their horizontal and vertical circumference (C_h and C_v) were measured with a measuring tape and volumes were estimated as $V = \frac{4}{3}\pi \left(\left(\frac{C_h}{2\pi}\right)^2 \times \frac{C_v}{2\pi}\right)$. All apples were weighed on a digital balance (Testus PFCD 6000, France) and sorted for weight:

1) Fruit from the Fuji cultivar consisted of 9 large (290 ± 23 g), 9 medium (185 ± 21 g) and 9 small (124 ± 27 g) apples (standard deviation corresponds to the dispersion of apple weights).

2) Fruit from the Ariane cultivar consisted of 6 medium (187 ± 12 g) and 3 small (133 ± 3 g) apples.

3) Fruit from the Jonagored cultivar consisted of 7 large (301 g ± 21 g) and 7 small (131 ± 16 g) apples.

Fuji and Ariane apples were grown at an experimental station (INRA, Angers) and were stored at 2°C for two months. Jonagored apples were obtained from a local organic farmer and stored at 2°C for five months.

Three samples were taken from the outer pericarp of 9 Fuji fruit (3 of each size) and 3 Ariane fruit (2 small and 1 medium) to measure water content (WC). WC was expressed as difference in weight after lyophylisation (Cosmos, Cryotec, Saint-Gély-du-Fesc, France).

2. MRI

1. Acquisition

MRI measurements were carried out on a 1.5T MRI scanner (Magnetom, Avanto, Siemens, Erlangen, Germany). Fruit were maintained at a constant temperature (20 ± 0.5°C) during acquisitions. The median planes of fruit (transverse section at middle height of fruit) were imaged with a pixel size of 1.19 mm^2, a slice thickness of 5 mm and a repetition time of 10 s. Two MRI sequences were performed: (i) a multi spin echo (MSE) sequence, with inter-echo spacing (ΔTE) of 7.1 ms, bandwidth 260 Hz, 1 scan and 512 echoes per echo train for estimation of T_2 and (ii) a multi gradient echo (MGE) sequence, with first echo time (TE1) of 2.8 ms and ΔTE 1.6 ms, bandwidth 1096 Hz, 12 echoes and 2 averages for estimation of T_2*.

2. Image processing

The T_2 and T_2* of apple parenchyma were computed by both pixel-by-pixel- and Region of Interest (ROI)- based approaches, as described above. First, a pixel-by-pixel approach was used to calculate T_2 and T_2* maps using Scilab software. Prior to fitting, seeds and core tissue around them together with the image background were masked using Otsu's thresholding method [36]. Mono-exponential T_2 maps were generated by performing pixel-to-pixel fitting via the Levenberg-Marquardt algorithm for chi-square minimization according to Eq. (2) (for i=1).

$$A(t) = \sum_{i=1}^{n} A_i \times e^{-\frac{t}{T_{2i}}} + const \qquad \text{Eq. (2)}$$

where t is the time, A_i the amplitude, T_{2_i} the transverse relaxation time of each component of the signal and *const* a value modeling the background offset. T_2* maps were computed as described for T_2 maps by substituting T_2 by T_2* in Eq. (2). Apparent microporosity maps were then computed from T_2 and T_2* maps according to Musse et al [19].

An ROI-based approach was used for estimation of multi-exponential relaxation parameters as it improved the Signal to Noise Ratio (SNR) [34]. ROIs were selected manually on homogeneous regions of mono-exponential T_2 maps using ImageJ software [37]. Regions with homogeneous mono-exponential T_2 were considered to have homogeneous multi-exponential T_2. The outer and inner parenchyma regions were selected to be close to the cuticle and the core, respectively (Fig. 2A). Selection of the outer parenchyma region avoided the first 2 mm region under the cuticle while selection of the inner parenchyma avoided the principal vascular bundles. The mean ROI signals were computed with ImageJ software for all the MSE images of the series and then fitted via the Levenberg-Marquardt algorithm for

chi-square minimization with TableCurve 2D software according to a tri-exponential decay curve (Eq. (2), i=3).

Values of the apparent microporosity used for statistics were estimated for the same ROIs as selected for estimation of multi-exponential T_2. In order to improve accuracy, T_2 and T_2* required for microporosity estimation were computed from the mean ROI intensity values rather than on a pixel-to-pixel basis.

3. Macro-vision imaging

1. Sampling and acquisition

Two days after MRI measurements, samples were taken from each fruit for macrovision imaging. The sampling protocol consisted of cutting a 1 cm slice, corresponding to twice the MRI virtual slice, at the equator of the fruit. Two 1 cm wide rectangular samples were then taken from the parenchyma (see Fig. 2B, gray line) and kept for two months at 4°C in a solution composed of 85:10:5% (v/v) ethanol 96%, formaldehyde 37% solution and acetic acid. Before imaging, tissue was rehydrated by placing the sample in successive ethanol baths (70%, 50% and 30%). Finally, 200 µm thick sections were cut from the middle of each sample using a vibrating blade microtome (MICROM, HM 650V, Microm International GmbH, Walldrof, Germany). They were degassed for 30 s under mild vacuum to remove remaining air bubbles. Sections were then imaged under water using a macro-vision system [35] comprising a CCD camera (Sony XC 8500 CE, Alliance Vision, Montélimar, France) fitted with a 50 mm lens (f 1:1.8 Nikon) and a 20 mm extension tube. Samples were back-lit using a fiber-optic ring-light supplied by Polytec (Pantin, France). The camera and lens were adjusted to observe a 10.7 mm x 14.4 mm area and images were digitized in 1620 x1220 pixels (pixels of 3.6x3.6 µm²).

2. Image processing

Two to four images per fruit were selected for image analysis. Images were considered for visual texture analysis according to both cell morphology and arrangement as they did not allow segmentation of cells. Image pixels were coded from 0 (black) to 255 (white). Gray level granulometric methods were applied using MatLab software to extract overall information concerning distribution of cell dimensions[35] on ROIs of the inner and outer regions of the parenchyma (see Fig. 2B). ROIs were selected (MatLab software) to correspond to MRI ROIs. Outer ROIs began at 1.5 mm from the cuticle and ended at 40% of the image length. Inner ROIs began at 60% of the image length from the cuticle and were 80% of the outer ROI length wide. By applying successive morphological closings on ROIs, dark objects on the image smaller than the structuring element were filled by the mean pixel value under the mask. A curve V_i was constructed by measuring the sum of gray levels after each closing step versus the size of the structuring element. The raw curve was normalized according to the sum of the initial ($V_{initial}$) and final (V_{final}) gray levels and written as:

$$g_i = (V_i - V_{i+1})/(V_{initial} - V_{final}) \qquad \textbf{Eq 3.}$$

where g(i) is the percentage of variation in gray level for the i^{st} step. The maximum size of the structuring element was set at 200 pixels, corresponding to 726 µm.

Horizontal and vertical linear structuring elements were applied, allowing analysis of cell dimensions in both directions. To compare the results from the different fruit, granulometric curves of gray levels were summarized for each direction by computing mean gray level sizes as the weighted sums bellow, thus providing the mean cell length (l) in the direction under consideration:

$$l = \exp\left(\sum_{i=1}^{imax} \frac{g(i)*\log(t_i)}{100}\right) \quad \textbf{Eq 4.}$$

where t_i is the size of the structuring element in µm and i_{max} the number of closing steps. This mean was considered to emphasize the smallest size.

Cell volume was estimated by considering the cells to be cylinders with the height (h) radial to the cuticle (cells were radially elongated) and the radius (r) parallel to the cuticle: $V = \pi r^2 \times h$.

As they were based on variations in gray level of pixels, granulometric curves did not measure the actual cell dimensions but a combination of cell dimensions and gray levels in which cells and pores could not be distinguished. Cell dimensions and consequently volume were therefore subject to uncertainty.

4. Statistics

ANOVA tests were performed using Statgraphics (Centurion) software to detect significant differences ($p < 0.01$) between measurements. The multifactor ANOVA test was applied to evaluate the differences between fruit sizes (small, medium and large) and between the inner and outer regions. Fruit size, region and cultivar, taking into account both cultivar and storage period, were used as factors. F-tests were performed on the results to assess the significance of the differences observed.

3 Results and discussion

1. Spatial distribution of T_2

Typical mono-exponential T_2 maps of Fuji and Ariane apples of different sizes are shown in Fig 3. The maps reflect the heterogeneity of the apple tissues. A pattern of radial variation was observed, with a progressive increase in T_2 values from the center of the fruit (~300 ms) to the region near the cuticle (~ 450 to 600 ms). The average T_2 in the inner parenchyma was about 350 ms, whereas it was about 600 ms in the outer parenchyma. In some apples, independently of fruit size or cultivar, the T_2 of the core and of the middle parenchyma were close and made it possible to distinguish the core from other tissues (e.g. medium Ariane fruit Fig 3). The vascular bundles were seen in some Fuji apples as their T_2 values contrasted from the surrounding tissue, the T_2 values being either higher or lower depending on the bundle (large Fuji, Fig 3). Vascular bundles are known to be composed of small cells and lignified cell walls. They should thus have lower T_2 values than the surrounding tissues and the contrast should generally emphasize dry bundles. The high T_2 (up to 800 ms) observed in the vascular bundle areas probably corresponded to water-filled large vessels. In some fruit, differences between fruit sides were observed (for example, differences between the top and bottom in the T_2 map for the Ariane cultivar, Fig. 3). Fruit development conditions such as sun exposure may have been at the origin of these differences between the two sides of the fruit.

Independently of fruit size, T_2 maps showed similar radial T_2 variations. However, when comparing fruit of different sizes, a global increase in T_2 value with fruit size was observed for parenchyma tissues. In particular, T_2 in the outer parenchyma region were about 450 ms for small fruit and up to 600 ms for large fruit.

The Jonagored cultivar (Supplementary data 1) showed a very similar global aspect, in terms of both the T_2 map pattern and the relationship between T_2 and fruit size.

In order to investigate sub-cellular water status and distribution, multi-exponential fitting was performed on the mean signal from the ROIs (Fig 2 A) corresponding to the outer and inner parenchyma. The results for all fruit are given in Table 1. In all cases, the multi-exponential T_2 parameters consisted of one short T_2 component (< 80 ms) with low relative intensity (< 10 %), an intermediate T_2 component (100 to 220 ms) with 14 to 20% of signal intensity and a long T_2 component (400 to 550 ms) representing 70 to 80% of the signal. For comparison, the mono-exponential value measured on the same ROIs (T_{2mono}) is given in Table 1. The standard deviations did not increase between the mono- and the multi-exponential results, indicating there was no degradation of the fit although seven variables were used for fitting instead of three. The relationship between T_{2mono} and T_{23} was linear, ($y = 1.12 \times x, r^2 = 0.97$) while none was found between T_{22} and T_{2mono} or T_{21} and T_{2mono}, demonstrating that the variations observed with mono-exponential T_2 mainly reflected changes in the vacuole compartment. However, T_{2mono} underestimated the T_2 of the vacuole compartment and did not provide access to other compartments.

Table 2 shows the results of the ANOVA test performed on mono- and multi-exponential data, with gray cells corresponding to significant variations. The mono-exponential T_2 was found to be discriminating for all parameters studied with a relatively high F-factor for the position, confirming observations from mono-exponential T_2 maps (Fig 3). In the case of the multi-exponential parameters, the most discriminating parameter depended on the variation considered. T_{23} had the most significant variations when comparing different positions, in agreement with the analysis performed on mono-exponential data, and reflecting a change in vacuole water status. The relative intensities of components 3 and 2 (I_{03}, I_{02}) also varied significantly between the inner and outer parenchyma. According to the attribution of the different T_2 components proposed by Snaar et al. [12], this means that the proportion of

vacuole water was higher and the proportion of cytoplasm water was lower in cells of the outer parenchyma than in cells of the inner parenchyma. Finally, T_{22} was also found to vary significantly between the inner and outer parenchyma, reflecting changes in the cytoplasm water status in addition to the proportion of water enclosed.

The parameters for fruit size were less affected. Only variations in T_{23} and I_{02} were significant, the relaxation time being lower and proportion of water enclosed in the cytoplasm being greater in the inner parenchyma.

On the other hand, variations between apple cultivars significantly affected all components of the multi-exponential T_2 signal, with relatively high F-factors which were not observed with the mono-exponential T_2. The parameters associated with the first component varied very significantly between cultivars but not between the outer and inner parenchyma tissue or between fruit of different sizes, suggesting that the amount of water and the relaxation time attributed to the cell wall were cultivar specific. Besides genetic factors, these differences might also have originated from pre-harvest conditions and storage time before measurement as the Jonagored cultivar was mainly responsible for these differences. Fruit from this cultivar were studied after 5 months' cold storage whereas the others were analyzed after 2 months' cold storage.

The water content did not explain variations in T_2 values: it was $82.8 \pm 1.3\%$ and $82.1 \pm 0.7\%$ in the outer parenchyma tissue of Fuji and Ariane fruit, respectively, and no significant variations were observed with size differences for the Fuji cultivar. Due to experimental constraints the water content was not measured for the inner parenchyma tissue but, in light of the T_2 variations observed, very significant changes in water content would be necessary, which were most unlikely [13].

As microporosity is also known to affect T_2, it was calculated to check its influence on the variations in T_2 observed.

2. Apparent microporosity and its impact on T_2

The heterogeneity of the apparent microporosity in apple tissues of Fuji and Ariane cultivars is depicted in Fig 4. Vascular bundles were the least porous parts of the fruit and were situated in a low microporosity region, highlighting the border between the core and the parenchyma tissues. Microporosity increased from this border to the outer parenchyma region and then decreased near the cuticle. For example, apparent microporosity values were about 15% of gas in the tissue for the core, from about 30 to 40 % for the parenchyma and about 10% in the vascular bundles of Ariane fruit. The same pattern was observed for the Jonagored cultivar (Supplementary data 1). The apparent microporosity measurements on ROIs from the outer and inner parenchyma are presented in Table 1 and confirm results from microporosity maps. Indeed, apparent microporosity in the outer parenchyma region was higher than in the inner parenchyma region. The result of an ANOVA-test (Table 2) showed this variation to be significant.

On looking at different fruit sizes, apparent microporosity of the outer parenchyma increased with the dimensions of fruit for all cultivars (Table 1). Microporosity of the inner parenchyma showed smaller variations with fruit size, in particular for Ariane fruit. In contrast, the greatest variations in the outer parenchyma were found between small and medium Ariane apples, although these fruit did not vary much in size. The microporosity of Fuji apples increased between the small and medium sizes but not between the medium and large sizes. These results confirmed the increase in apparent microporosity reported with fruit size for Royal Gala apples [6] and also highlighted that maximum microporosity can be reached, according to the cultivar. This upper limit may explain the absence of variations in microporosity in Empire apples reported by Goffinet et al. [8]: as fruit thinning had been used

to increase fruit size, the different sizes studied may have corresponded to fruit which had already reached a maximum and constant microporosity.

Herremans et al. [7] used X-Ray micro-CT to measure microporosity in three regions of Braeburn apples: Region 1, corresponding to a mix of outer parenchyma and under-cuticle regions as defined in the present paper, Region 2, corresponding to a mix of outer and inner parenchyma tissue, and Region 3, corresponding to the core tissue. They reported apparent microporosity values of 15, 18 and 19.9% for regions 1 to 3, respectively. Our results are in good agreement with these findings. The core tissues of Ariane, Fuji and Jonagored apples had the lowest microporosity; the low microporosity observed in the under-cuticle region in the three cultivars support the lower microporosity of Region 1 compared to the middle cortex reported in Braeburn apples [6]. The microporosity of Fuji apples estimated using X-Ray microtomography was 29% for an under-cuticle/outer parenchyma region [38], which was lower than our measurements (39% for outer parenchyma). However, numerous aspects should be considered when comparing microporosity values calculated from different techniques. First, from a biological point of view : studies on different apple cultivars have shown that microporosity values are cultivar dependent and vary according to pre- and post-harvest conditions and maturity [3,7,8]. For example, the microporosity estimated in the middle parenchyma tissue of Braeburn and Jonica apples was 10 % and 16%, respectively, the former increasing during 3 months storage to 18%, the latter decreasing to 14% [3]. The measurement method is another factor: X-Ray microtomography values depend on the measurement protocol. The microporosity varied between 19 and 29% in parenchyma tissue of Jonagold apples depending on the image resolution and representative elementary volume used for the analysis [39]. Similar variations can be expected for MRI since the apparent microporosity depends on the main magnetic field strength [18]. Comparison of microporosity values from different experiments is therefore difficult, especially as the

regions considered for microporosity quantification differ between studies. To circumvent this last limitation, MRI represents a more suitable approach for the analysis of fruit structure as it allows the measurement of the spatial distribution of microporosity in a whole fruit.

Both apparent microporosity and T_2 maps were characterized by specific radial variations (Figs. 3 and 4) with relatively similar aspects. The T_{23}, T_{22} and microporosity values were higher in the outer than in the inner parenchyma region (Table 1). Since higher microporosity induces lower T_2 [18], microporosity was thus not the main factor explaining the variations in T_{22} and T_{23}. However, as microporosity was considerably higher in the outer than in the inner parenchyma, the T_2 and especially T_{23} value ranges were probably underestimated and differences in relaxation times between the parenchyma were very probably reduced. Defraeye et al. [33] used a high field MRI scanner (11.7 T) and an MSE sequence with a 7 ms echo time very close to the echo time we used (7.1 ms). They found relatively low T_2 values (between 25 and 40 ms) that were higher in the inner parenchyma than in the outer parenchyma. This discordance with our results is probably due to the effects of microporosity-induced susceptibility inhomogeneities at high field and the relatively long TE used [18,34]. As microporosity was found to have more impact on T_2 in tissue rich in air [19], higher microporosity of the outer parenchyma shortened T_2 values, resulting in lower T_2 values than for the inner parenchyma. This explanation is supported by their low T_2 values, as the T_2 of porous fruit was shown to decrease with the increase in the magnitude of the main magnetic field [19]. The T_2 values measured by Defraeye et al. therefore seem to reflect changes in microporosity rather than changes in water status.

3. Tissue histology and MRI measurements

Fig 5 shows the macrovision images of parenchyma of Fuji and Ariane cultivars with zooms on the regions corresponding to the ROIs used for MRI analyses in the outer and inner parenchyma tissue. The parenchyma tissue was heterogeneous in terms both of cell size and shape. Under the cuticle, an approximately 2 mm wide region was composed of small cells with sizes increasing with distance from the cuticle. This region matched the first peripheral pixels of T_2 and microporosity maps (Figs. 3 and 4) characterized by lower apparent microporosity and T_2 values than the rest of the parenchyma tissue. As the cells were small, there was more light diffusion on the image and the region appears whiter compared to other regions. The outer parenchyma tissue was characterized by round cells of roughly 180 µm. For most fruit studied, the cells tended to elongate in a direction perpendicular to the cuticle when the distance from the cuticle increased. Some inner parenchyma tissues included non-elongated cells (Fig. 5 D). The elongated cells observed close to the vascular bundles were often oriented (Fig. 5, A, B) in the direction of the closest vascular bundle. The border between the parenchyma and core tissues (Fig. 5 A, B and C, arrows) was a compact tissue with smaller cells, appearing slightly brighter as in mature fruit [40,41]. These findings agree with previous studies on apple parenchyma histology, showing the tissue cell morphology dependency on location [2,3,42]. They highlighted heterogeneity of the higher tissue structure of the inner parenchyma compared to the outer parenchyma tissue for fruit of the same size and cultivar. When comparing fruit of different sizes, large fruit appeared visually to be richer in intercellular spaces in the outer part of the pericarp (Fig. 5). The cell shape of small fruit tended to be more heterogeneous in the inner parenchyma tissue.

The cell morphology of the Jonagored cultivar was similar and varied in the same way between the outer and inner regions (Supplementary data 2).

The image texture algorithms used to analyze macrovision images yielded size distributions of dark objects, which were used to estimate mean cell sizes, assuming that dark

objects were all cells. Cell volume was estimated by computing the estimations of horizontal and vertical cell sizes (Eq. (4)). An ANOVA revealed a significant variation in cell volume between the inner and the outer parenchyma tissues ($F = 18.40$, $p = 0.000$), the outer parenchyma cells being larger than the inner parenchyma cells, and between the outer parenchyma of fruit of different sizes ($F = 10.17$, $p = 0.000$). The tissue heterogeneity within apple cultivars reduced the differences between the different apple varieties. The heterogeneity was greater in the inner parenchyma tissue due to cell elongation and the presence of vascular bundles. Further analysis was therefore focused on the outer parenchyma. As the thickness of the section was 200 µm (although cell size varied), fruit with small cells had more cell layers, which resulted in underestimation of cell size for such fruit (Fig. 5C). However, underestimation was limited as the granulometric analysis was based on gray levels.

Fig. 6 depicts cell volume of the outer parenchyma region as a function of fruit weight. As the relationship between weight (w) and volume (V) was linear ($w = 1.18 \times V$, $r^2 = 0.93$), fruit weight was used instead of estimation of fruit volume, the measurement of which was less precise. The relationship between cell size and fruit size depended on the cultivar being studied. The graph shows that cell size slightly increased with fruit size only for the Fuji cultivar and in the small and medium fruit range. These results confirm that the size of the fruit can depend on the cell number and size [4,5], or on both parameters, and underline the significant dependency of this relationship on cultivars. ANOVA performed only on the Fuji cultivar resulted in an F-value of 20.64, confirming the relationship between cell volume and fruit size.

According to Van der Weerd et al. [16] the relaxation rate of the third component ($1/T_{23}$) depends on the vacuole size (Eq. (1)), the latter being approximated by cell size in vacuolated

cells. The relationship between $1/T_{23}$ and cell size was investigated for the outer parenchyma of Fuji cultivar, for which both T_{23} and cell volume differed between apples of different sizes. There was considerable data dispersion and consequently a relatively weak linear relationship was established ($r^2 = 0.59$). The relatively weak association between $1/T_{23}$ and cell dimensions was at least in part linked to the narrow range of cell sizes found in this study. Indeed, Van der Weerd et al. studied pearl millet and maize stems with approximate cell radii of a few micrometers to a hundred micrometers (factor 20) while the radii of apple cells of this study ranged from 145 µm to 220 µm (factor 1.5). Nevertheless, the intercept of the fitted line in Fig. 7, corresponding to the bulk T_2 of the vacuole, was about 2.12 s, as expected (T_2 for water at 20°C was 2.08 s) and the slope of the line linked to the magnetization sink strength parameter was $H = 9.0 \times 10^{-5}\, m.s^{-1}$. The value of H obtained in this study was higher than the values observed on maize and pearl millet ($2.8 \times 10^{-5}\, m.s^{-1}$ and $4.0 \times 10^{-5}\, m.s^{-1}$, respectively) [16], on Cameron and Quest tomatoes (1.1×10^{-5} and 0.5×10^{-5}, respectively) [43] and on Granny Smith cultivar apples (1.0×10^{-5}) [10]. However, differences in protocols may be at the origin of these variations.

First, Van der Weerd et al. [16] considered the mono-exponential T_2 to be the vacuolar T_2 while the vacuolar T_2 in the present study was estimated from the multi-exponential relaxation. A T_2 computed with a mono-exponential fit as in Van der Weerd's study resulted in a higher H value ($H_{mono} = 10.0 \times 10^{-5}\, m.s^{-1}$). Furthermore, measurements in the present study were performed on a higher field and with longer TE, thus underestimating T_2 because of the impact of microporosity [18,34]. Using a relationship established between

NMR (20 MHz, TE = 0.1 ms) T_2 and MRI T_2 [34], new values of H could be approximated: $H_{NMR} = 3.8 \times 10^{-5}\, m.s^{-1}$ and $H_{NMR,mono} = 4.0 \times 10^{-5}\, m.s^{-1}$. The latter values are closer to each other than the original values, indicating that the porosity effect on T_2 was corrected. Moreover, the latter values are in the range of H values from previous studies. However, as illustrated by the change in H value between the MRI and NMR methods, it is difficult to compare the values obtained by different methods.

On the other hand, when looking at the whole data set, including both inner and outer parenchyma data, the relationship between cell dimensions and T_{23} (Eq. (1)) no longer exists even for the Fuji cultivar. This result indicates that variations in T_2 within parenchyma cannot be explained only by changes in cell sizes. Other phenomena may be the causes of these variations [10]. For instance, the permeability of cell membranes may vary inside tissues and between cultivars. Further, different plant cell components (sugars, proteins and other macromoleculs) may alter relaxation times via chemical exchange [11]. Raffo et al. [44] investigated the relationship between transverse relaxation and changes in chemical composition occurring during ripening of banana fruit. They demonstrated that an increase in T_2 was linked to the decrease in starch concentration, while the increasing sugar concentration produced only minor effects. On the other hand, studies on kiwifruit [45] or Asian persimmon [46] did not shown any obvious relationship between the monoexponential T_2 relaxation time and the tested cell solutes. The impact of the chemical composition on the T_2 relaxation has therefore to be elucidated.

4 Conclusion

We demonstrated in this study that a combined quantitative MRI approach based on multi-exponential T_2 and porosity measurements provided better discrimination between

tissues than the previous mono-exponential T_2 map approaches. Indeed, multi-exponential fitting allowed investigation of water status and distribution at the subcellular level. Moreover, a reliable interpretation of T_2 was ensured, taking into account tissue porosity. It was also shown that measurements at a relatively low magnetic field (1.5 T) make it more possible to discriminate tissues than measurements performed at a high field where strong effects of magnetic susceptibility prevent reliable T_2 mapping.

Investigating apple fruit on a millimeter scale using mono-exponential T_2 and porosity maps confirmed the heterogeneous structure of apple parenchyma tissue and identified two homogeneous regions in parenchyma (inner and outer parenchyma). Differences between the regions were then assessed for all the parameters measured (multi-exponential relaxation times and associated relative amplitudes, apparent microporosity and cell size) for the three cultivars, providing information at the subcellular and tissue level. As relaxation components were linked to cell compartments, these differences were interpreted in terms of modification of the water distribution between the vacuole and the cytoplasm and modification of membrane permeability. Moreover, a difference in the T_2 attributed to the cell wall (T_{21}), observed between cultivars suggests that MRI measurements could be used for the characterization of tissue texture as this might be related to turgor pressure, supported by the cell wall.

Multi-exponential fitting was performed on ROIs in this study. The challenge for better characterization of fruit tissue will be to apply the same approach to individual pixels in order to compute maps corresponding to the T_2 and associated signal intensity of the different components. This would require a higher signal to noise ratio and probably improving the image processing method used.

As mentioned above, specific variations were also observed between cultivars in addition to the relaxation times and porosity distributions inside fruit. The same pre-harvest conditions, maturity at harvest and storage conditions (shown to affect porosity and relaxation times) for all cultivars would be required to generalize these results. Further investigations will therefore be necessary to assess specific cultivar features.

As T_2 differences were also observed between fruit of different sizes, the results of MRI and histological measurements were compared to investigate the sources of these variations. These showed that variation in cell size might be linked to the vacuole-associated T_2, as correlations were established between cell size and T_{23}. However, compartment size only partially explains the variations in T_2 and several other parameters may be the causes of these variations. Measuring and mapping the diffusion coefficients, as well as measuring concentrations of cell solutes could contribute to the better understanding of the signal.

The MRI mapping of apparent microporosity in this study and determination of the spatially resolved multi-exponential T_2 relaxation demonstrated the high value of these approaches in the non-destructive determination of apple microstructure. These methods will be particularly valuable for the sampling of specific tissues to further investigations into the origins of T_2 contrast and the impact of tissue microstructure on fruit texture.

Acknowledgments: This work was financed in part by the AI-FRUIT Pays de la Loire Research Program. GW was supported in part by a scholarship from the Pays de la Loire and Bretagne regions.

LEGENDS:

Figure 1: Diagram of the equatorial plane of an apple showing the internal structure of the fruit.

Figure 2: MRI T_2-weighted image showing (A) the regions of interest used for MRI multi-exponential fitting corresponding to the outer (white) and inner (black) parenchyma tissue and (B) the region of sampling used for the macrovision imaging (gray) with the outer (white) and inner (black) areas used for granulometric analysis.

Figure 3: Mono-exponential T_2 maps of Ariane and Fuji cultivars of different sizes. The reader is referred to the web version of this article for interpretation of the references to color in this figure legend.

Figure 4: Apparent microporosity maps of Ariane and Fuji cultivars of different sizes. The reader is referred to the web version of this article for interpretation of the references to color in this figure legend.

Figure 5: Macrovision images of two sizes of Fuji (A-B) and Ariane (C-D) cultivars, corresponding to the whole parenchyma region, and zoom-in on regions in the inner and outer parenchyma as analyzed using granulometric methods. Scale bar is 2 mm.

Figure 6: Plot of cell volume as a function of fruit weight for the three cultivars studied.

Figure 7: Plot of the vacuole compartment-associated T_2 (T_{23}) as a function of cell dimensions for the Fuji cultivar. The linear fit is indicated as a line ($r^2 = 0.60$).

SUPPLEMENTARY DATA:

Figure 1: Monoexponential T2 (A) and apparent microporosity (B) maps of Jonagored cultivar for the different sizes. The reader is referred to the web version of this article for interpretation of the references to color in this figure legend.

Figure 2: Macrovision images of two sizes of Jonagored cultivar corresponding to the whole parenchyma region and zoom-in on regions in the inner and outer parenchyma as analyzed using granulometric methods. Scale bar is 2 mm.

REFERENCES

1. Bourne MC. Food texture and viscosity: concept and measurement; 1982. xii + 325pp. p.
2. Khan AA, Vincent JFV. Anisotropy of apple parenchyma. J Sci Food Agric 1990;52(4):455-466.
3. Schotsmans W, Verlinden BE, Lammertyn J, Nicolai BM. The relationship between gas transport properties and the histology of apple. J Sci Food Agric 2004;84(10):1131-1140.
4. Harada T, Kurahashi W, Yanai M, Wakasa Y, Satoh T. Involvement of cell proliferation and cell enlargement in increasing the fruit size of Malus species. Sci Hortic 2005;105(4):447-456.
5. Malladi A, Hirst PM. Increase in fruit size of a spontaneous mutant of 'Gala' apple (Malusxdomestica Borkh.) is facilitated by altered cell production and enhanced cell size. J Exp Bot 2010;61(11):3003-3013.
6. Volz RK, Harker, F.R., Hallet, I.C. and Lang, A. Development of texture in apple fruit - A biophysical perspective. Acta Hort 2004;636:473-479.
7. Herremans E, Verboven P, Bongaers E, Estrade P, Verlinden BE, Wevers M, Hertog M, Nicolai BM. Characterisation of 'Braeburn' browning disorder by means of X-ray micro-CT. Postharvest Biol Technol 2013;75:114-124.
8. Goffinet MC, Robinson TL, Lakso AN. A comparison of 'empire' apple fruit size and anatomy in unthinned and hand-thinned trees. J Horticult Sci 1995;70(3):375-387.
9. Van As H, van Duynhoven J. MRI of plants and foods. J Magn Reson 2013;229:25-34.
10. Van As H. Intact plant MRI for the study of cell water relations, membrane permeability, cell-to-cell and long distance water transport. J Exp Bot 2007;58(4):743-756.
11. Hills BP, Duce SL. The influence of chemical and diffusive exchange on water proton transverse relaxation in plant tissues. Magn Reson Imaging 1990;8(3):321-331.
12. Snaar JEM, Van as H. Probing water compartments and membran-permeability in plant-cells by H-1-NMR relaxation measurements. Biophysical Journal 1992;63(6):1654-1658.
13. Hills BP, Remigereau B. NMR studies of changes in subcellular water compartmentation in parenchyma apple tissue during drying and freezing. Int J Food Sci Technol 1997;32(1):51-61.
14. Sibgatullin TA, Anisimov AV, de Jager PA, Vergeldt FJ, Gerkema E, Van As H. Analysis of diffusion and relaxation behavior of water in apple parenchymal cells. Biofizika 2007;52(2):268-276.
15. Brownstein KR, Tarr CE. Importance of classical diffusion in NMR studies of water in biological cells. Physical Review A 1979;19(6):2446-2453.
16. van der Weerd L, Claessens M, Ruttink T, Vergeldt FJ, Schaafsma TJ, Van As H. Quantitative NMR microscopy of osmotic stress responses in maize and pearl millet. J Exp Bot 2001;52(365):2333-2343.
17. Edzes HT, van Dusschoten D, Van As H. Quantitative T-2 imaging of plant tissues by means of multi-echo MRI microscopy. Magnetic Resonance Imaging 1998;16(2):185-196.
18. Donker HCW, Van As H, Edzes HT, Jans AWH. NMR imaging of white button mushroom (Agaricus bisporis) at various magnetic fields. Magn Reson Imaging 1996;14(10):1205-1215.

19. Musse M, De Guio F, Quellec S, Cambert M, Challois S, Davenel A. Quantification of microporosity in fruit by MRI at various magnetic fields: comparison with X-ray microtomography. Magn Reson Imaging 2010;28(10):1525-1534.
20. Chen P, McCarthy MJ, Kauten R. NMR for Internal Quality Evaluation of Fruits and Vegetables. Transactions of the ASAE 1989;32(5):1747-1753.
21. McCarthy MJ, Zion B, Chen P, Ablett S, Darke AH, Lillford PJ. Diamagnetic susceptibility changes in apple tissue after bruising. J Sci Food Agr 1995;67(1):13-20.
22. Cho BK, Chayaprasert W, Stroshine RL. Effects of internal browning and watercore on low field (5.4 MHz) proton magnetic resonance measurements of T-2 values of whole apples. Postharvest Biol Technol 2008;47:81-89.
23. Melado-Herreros A, Munoz-Garcia MA, Blanco A, Val J, Fernandez-Valle ME, Barreiro P. Assessment of watercore development in apples with MRI: Effect of fruit location in the canopy. Postharvest Biol Technol 2013;86:125-133.
24. Clark CJ, MacFall JS, Bieleski RL. Loss of watercore from 'Fuji' apple observed by magnetic resonance imaging. Sci Hortic 1998;73(4):213-227.
25. Clark CJ, Burmeister DM. Magnetic resonance imaging of browning development in 'Braeburn' apple during controlled-atmosphere storage under high CO2. Hortscience 1999;34(5):915-919.
26. Gonzalez JJ, Valle RC, Bobroff S, Viasi WV, Mitcham EJ, McCarthy MJ. Detection and monitoring of internal browning development in 'Fuji' apples using MRI. Postharvest Biol Technol 2001;22(2):179-188.
27. Suzuki T, Sasaki, Y., Kuroda, K. and Oosawa, K. Histological features and dynamics of the development of watercore in apple (*Malus Domestica*) fruit. 2003;628:495-500.
28. Herremans E, Melado-Herreros A, Defraeye T, Verlinden B, Hertog M, Verboven P, Val J, Fernández-Valle ME, Bongaers E, Estrade P, Wevers M, Barreiro P, Nicolaï BM. Comparison of X-ray CT and MRI of watercore disorder of different apple cultivars. Postharvest Biol Technol 2014;87(0):42-50.
29. James HJ, Jobling JJ. Contrasting the structure and morphology of the radial and diffuse flesh browning disorders and CO2 injury of ‘Cripps Pink’ apples. Postharvest Biol Technol 2009;53(1–2):36-42.
30. Barreiro P, Moya A, Correa E, Ruiz-Altisent M, Fernandez-Valle M, Peirs A, Wright KM, Hills BP. Prospects for the rapid detection of mealiness in apples by nondestructive NMR relaxometry. Appl Magn Reson 2002;22(3):387-400.
31. Barreiro P, Ortiz C, Ruiz-Altisent M, Ruiz-Cabello J, Fernandez-Valle ME, Recasens I, Asensio M. Mealiness assessment in apples and peaches using MRI techniques. Magnetic Resonance Imaging 2000;18(9):1175-1181.
32. Barreiro P, Ruiz-Cabello J, Fernandez-Valle ME, Ortiz C, Ruiz-Altisent M. Mealiness assessment in apples using MRI techniques. Magnetic Resonance Imaging 1999;17(2):275-281.
33. Defraeye T, Lehmann V, Gross D, Holat C, Herremans E, Verboven P, Verlinden BE, Nicolai BM. Application of MRI for tissue characterisation of ‘Braeburn’ apple. Postharvest Biol Technol 2013;75(0):96-105.
34. Adriaensen H, Musse M, Quellec S, Vignaud A, Cambert M, Mariette F. MSE-MRI sequence optimisation for measurement of bi- and tri-exponential T2 relaxation in a phantom and fruit. Magnetic Resonance Imaging 2013(0).
35. Devaux M-F, Bouchet B, Legland D, Guillon F, Lahaye M. Macro-vision and grey level granulometry for quantification of tomato pericarp structure. Postharvest Biol Technol 2008;47(2):199-209.
36. Otsu N. Threshold selection method from gray-level histograms. IEEE Trans Syst Man Cybern 1979;SMC-9(1):62-66.

37. Schneider CA, Rasband WS, Eliceiri KW. NIH Image to ImageJ: 25 years of image analysis. Nat Meth 2012;9(7):671-675.
38. Moller SM, Travers S, Bertram HC, Bertelsen MG. Prediction of postharvest dry matter, soluble solids content, firmness and acidity in apples (cv. Elshof) using NMR and NIR spectroscopy: a comparative study. Eur Food Res Technol 2013;237(6):1021-1024.
39. Mendoza F, Verboven P, Mebatsion HK, Kerckhofs G, Wevers M, Nicolai B. Three-dimensional pore space quantification of apple tissue using X-ray computed microtomography. Planta 2007;226(3):559-570.
40. Esau K. Anatomy of seed plants. Anatomy of seed plants; 1960.
41. Fisk EL, Millington W.F. Atlas of plant morphology. Portfolio II: Photomicrographs of flower, fruit and seed. Minneapolis, Minnesota: Burgess; 1962.
42. Bain JM, Robertson RN. The physiology of growth in apple fruits. I. Cell size, cell number, and fruit development. Australian journal of scientific research Ser B: Biological sciences 1951;4(2):75-107.
43. Duval F, Cambert M, Mariette F. NMR study of tomato pericarp tissue by spin-spin relaxation and water self-diffusion. Appl Magn Reson 2005;28(1-2):29-40.
44. Raffo A, Gianferri R, Barbieri R, Brosio E. Ripening of banana fruit monitored by water relaxation and diffusion H-1-NMR measurements. Food Chem 2005;89(1):149-158.
45. Clark CJ, Drummond LN, MacFall JS. Quantitative NMR imaging of kiwifruit (Actinidia deliciosa) during growth and ripening. J Sci Food Agric 1998;78(3):349-358.
46. Clark CJ, MacFall JS. Quantitative magnetic resonance imaging of 'Fuyu' persimmon fruit during development and ripening. Magn Reson Imaging 2003;21(6):679-685.

Figure 1

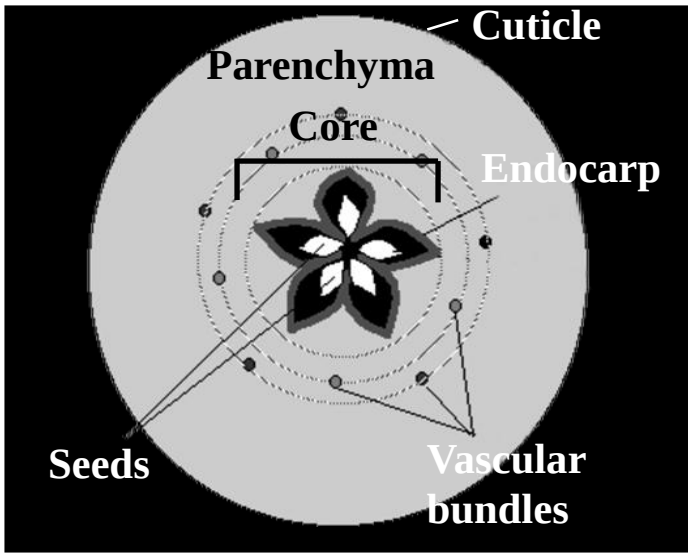

Figure 2

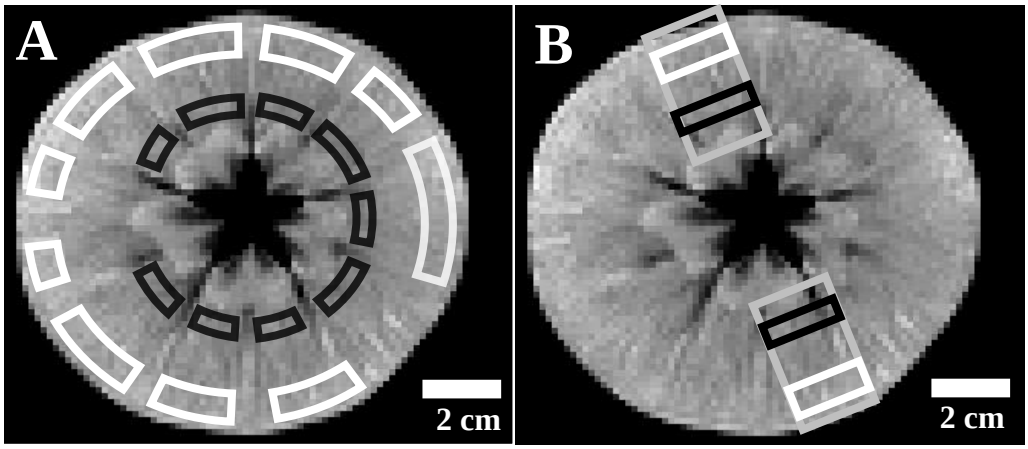

Figure 3

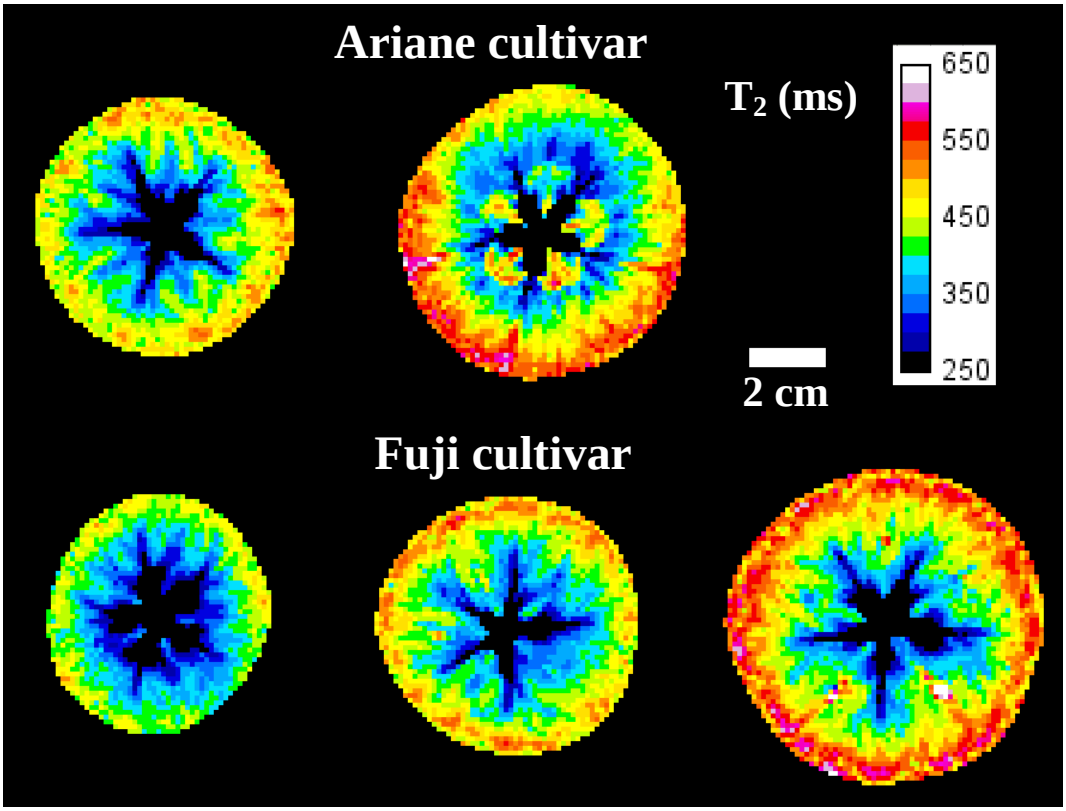

Figure 4

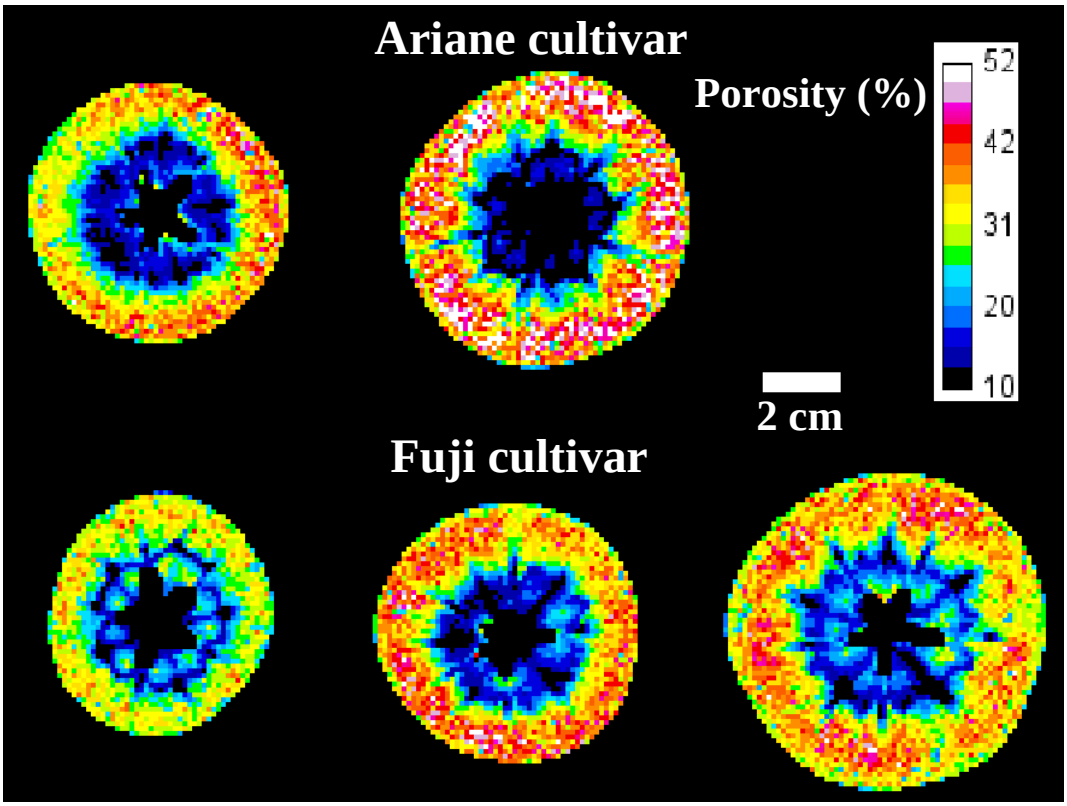

Figure 5

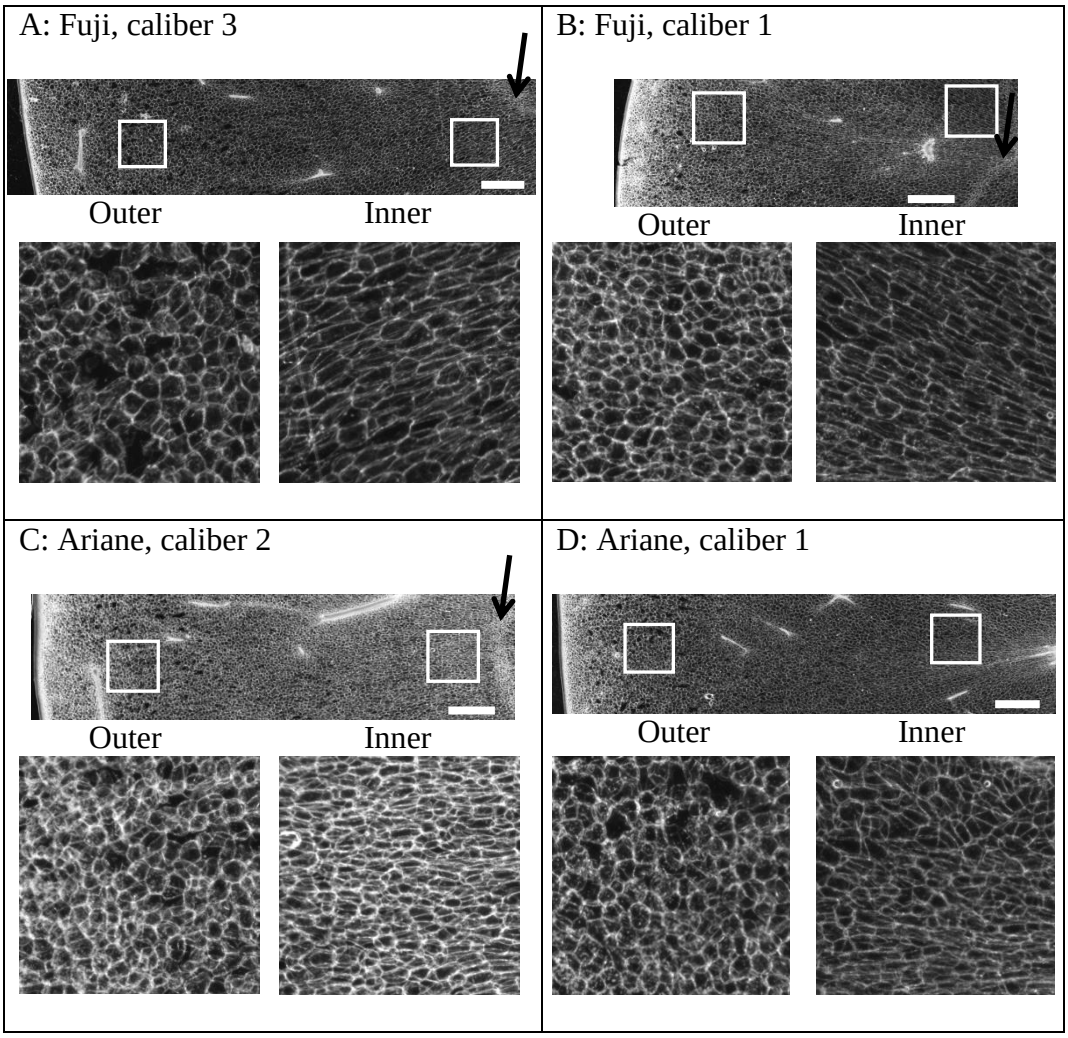
A: Fuji, caliber 3
Outer
Inner
B: Fuji, caliber 1
Outer
Inner
C: Ariane, caliber 2
Outer
Inner
D: Ariane, caliber 1
Outer
Inner

Figure 6

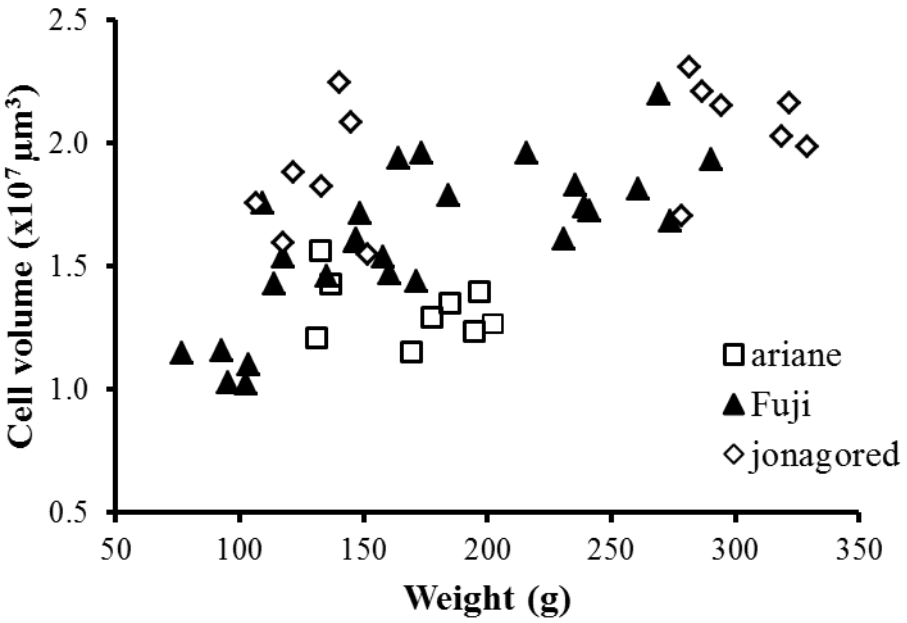
2.5
2.0
1.5
1.0
0.5
Cell volume (x10^7 µm^3)
50
100
150
200
250
300
350
Weight (g)
ariane
Fuji
jonagored

Figure 7

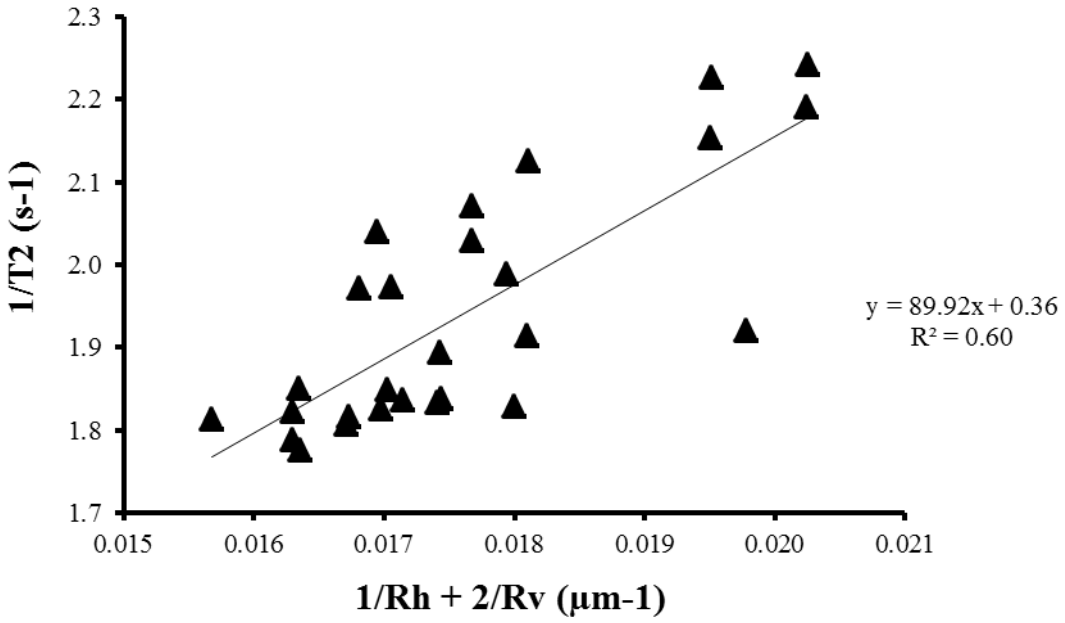
2.3
2.2
2.1
2.0
1.9
1.8
1.7
1/T2 (s-1)
0.015
0.016
0.017
0.018
0.019
0.020
0.021
1/Rh + 2/Rv (µm-1)
y = 89.92x + 0.36
R² = 0.60

supplementary figure 1

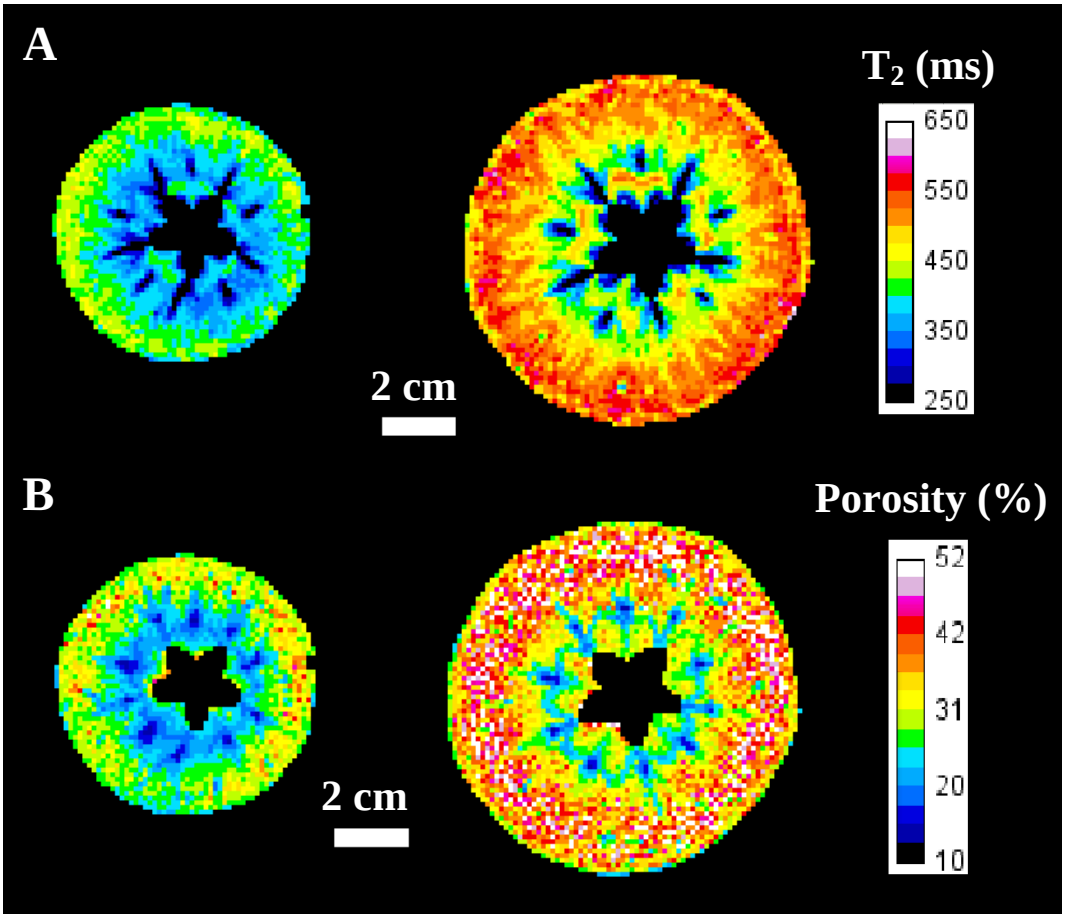

supplementary figure 2

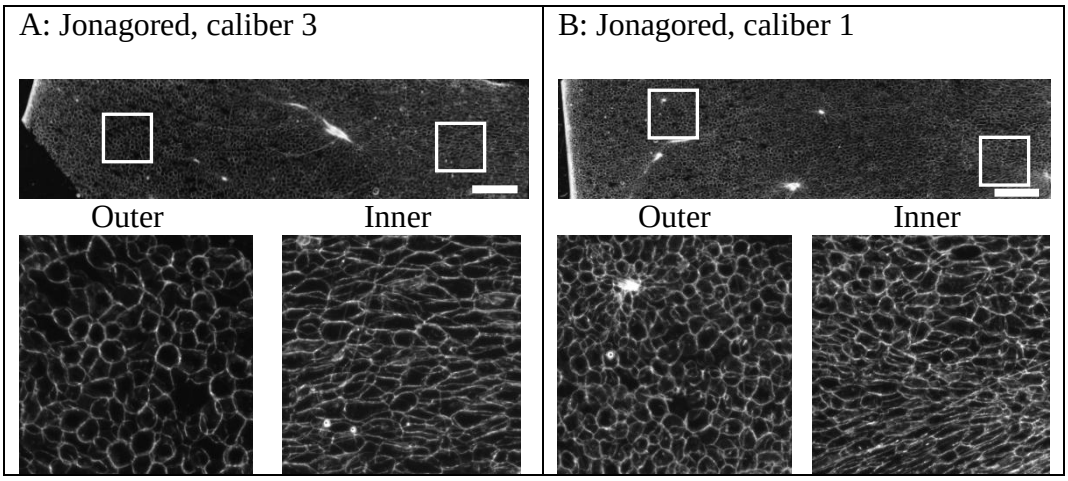

Table 1

Table 1. Multi-exponential fit parameters and estimations of microporosity in parenchyma of apple

A. Outer Parenchyma

Cultivar	Size	I_{01} [%]	T_{21} [ms]	I_{02} [%]	T_{22} [ms]	I_{03} [%]	T_{23} [ms]	T_{2mono} [ms]	Porosity [%]
Ariane	M	3±0	31±4	17±0	139±9	80±1	531±22	469±23	42±4
	S	3±0	22±2	15±1	129±8	82±1	524±26	469±18	34±2
Fuji	L	3±0	25±2	14±1	136±4	82±1	549±7	494±5	39±2
	M	3±0	23±2	14±1	126±6	83±1	522±24	471±23	39±2
	S	2±1	20±4	14±0	115±11	83±1	482±34	437±30	33±3
Jonagored	L	7±4	65±22	19±1	214±69	74±5	512±30	451±22	34±4
	S	7±4	67±21	14±3	187±41	78±2	465±24	420±24	28±6

B. Inner Parenchyma

Cultivar	Size	I_{01} [%]	T_{21} [ms]	I_{02} [%]	T_{22} [ms]	I_{03} [%]	T_{23} [ms]	T_{2mono} [ms]	Porosity [%]
Ariane	M	3±0	18±4	21±1	104±5	76±1	407±26	351±24	28±6
	S	3±0	19±4	17±0	107±4	80±0	451±20	401±17	28±2
Fuji	L	3±1	18±4	18±1	113±8	79±1	465±25	410±22	26±3
	M	3±0	18±3	17±1	104±7	80±1	439±26	390±22	28±2
	S	3±1	16±3	16±1	98±6	81±1	410±22	368±20	25±4
Jonagored	L	8±4	57±19	19±2	175±47	72±3	454±21	395±17	25±3
	S	14±4	80±12	14±6	210±50	71±6	414±24	362±24	19±4

Results of the fit using the Levenberg-Marquardt algorithm are presented for outer (A) and inner (B) parenchyma ROIs of each cultivar.

Table 2

Table 2. Analysis of variance for MRI parameters with position within parenchyma, size and fruit

	I_{01}		T_{21}		I_{02}		T_{22}		I_{03}		T_{23}		T_{2mono}		Porosity	
	F	P	F	P	F	P	F	P	F	P	F	P	F	P	F	P
Position	3.3	0.07	4.8	0.03	25.2	0.00	11.9	0.00	32.6	0.00	198.6	0.00	230.8	0.00	203.5	0.00
Caliber	2.2	0.11	1.3	0.27	16.3	0.00	0.5	0.60	3.6	0.03	32.8	0.00	24.2	0.00	20.0	0.00
Cultivar	64.2	0.00	166.1	0.00	10.8	0.00	65.9	0.00	77.2	0.00	7.1	0.00	10.9	0.00	12.4	0.00

F-test value (F) and probability for the null hypothesis (P) are presented for each MRI parameter.